Inorganic Chemistry

pubs.acs.org/IC Article

Vacancy-Driven Disorder and Elevated Dielectric Response in the Pyrochlore $Pb_{1.5}Nb_2O_{6.5}$

Uyen Dang, Jake O'Hara, Hayden A. Evans, Daniel Olds, Juan Chamorro, Daniel Hickox-Young, Geneva Laurita,* and Robin T. Macaluso*

Cite This: *Inorg. Chem.* 2022, 61, 18601−18610 Read Online

ACCESS | Metrics & More | Article Recommendations | Supporting Information

ABSTRACT: Lone pair-driven distortions are a hallmark of many technologically important lead (Pb)-based materials. The role of Pb^{2+} in polar perovskites is well understood and easily manipulated for applications in piezo- and ferroelectricity, but the control of ordered lone pair behavior in Pb-based pyrochlores is less clear. Crystallographically and geometrically more complex than the perovskite structure, the pyrochlore structure is prone to geometric frustration of local dipoles due to a triangular arrangement of cations on a diamond lattice. The role of vacancies on the O′ site of the pyrochlore network has been implicated as an important driver for the expression and correlation of stereochemically active lone pairs in pyrochlores such as $Pb_2Ru_2O_{6.5}$ and $Pb_2Sn_2O_6$. In this work we report on the structural, dielectric, and heat capacity behavior of the cation- and anion-deficient pyrochlore $Pb_{1.5}Nb_2O_{6.5}$ upon cooling. We find that local distortions are present at all temperatures that can be described by cristobalite-type cation ordering, and this ordering persists to longer length scales upon cooling. From a crystallographic perspective, the material remains disordered and does not undergo an observable phase transition. In combination with density function calculations, we propose that the stereochemical activity of the Pb^{2+} lone pairs is driven by proximity to O′ vacancies, and the crystallographic site disorder of the O′ vacancies prohibits long range correlation of lone pair-driven distortions. This in turn prevents a low-temperature phase transition and results in an elevated dielectric permittivity across a broad temperature range.

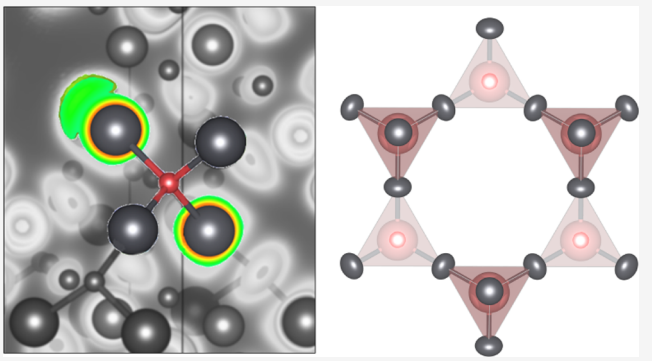

INTRODUCTION

Pyrochlores have been extensively studied for a variety of technologically important properties, including high electrical conductivity,[1,2] ferroelectricity,[3] photocatalysis,[4,5] frustrated magnetism,[6−8] ordered magnetism,[9] photoluminescence,[10] and ionic conductivity.[11−14] Some pyrochlores, such as $(Bi_{1.5}Zn_{0.5})(Nb_{1.5}Zn_{0.5})O_7$ (BZN),[15] $Bi_2Ti_2O_7$,[16−19] and mixed-anion $Pb_2Ti_2O_{5.4}F_{1.2}$,[20] have attracted considerable attention as high-κ materials, where the large dielectric constants are closely tied to short-range displacements of the metal cations. Of particular recent interest are pyrochlores where dipole moments are geometrically frustrated within a topological lattice, leading to spin (magnetic dipoles)[21] and charge (electric dipoles)[15] ice behavior.

The ideal pyrochlore with the chemical formula $A_2B_2O_7$ (often written $A_2B_2O_6O'$) is described with the cubic $Fd\bar{3}m$ space group.[22] The A cations (typically a +2 or +3 cation) and B cations (typically a +5 or +4 cation) are located on separate but interpenetrating A_2O' and B_2O_6 frameworks, illustrated in Figure 1a. The A_2O' framework consists of corner-linked $A_{4/2}O'$ tetrahedra, and the B_2O_6 framework consists of BO_6 octahedra. These octahedra are corner linked, forming a six-membered ring (Figure 1b), where the A-site cations are ideally positioned at the 16d site at the center of the BO_6 ring and linearly coordinated to the O′ anions perpendicular to the ring. This ring structure creates a channel within the overall structure, and the size of this structure allows for flexibility of atom positions; for example, the A cation can shift toward the ring into the 96g site,[17,19,23−26] and the O′ can shift above and below the ring plane to the 32e site.[17,22] The rigid channel structure additionally allows for compositional flexibility in the form of vacancies on both A and O′ sites.[22]

The arrangement of dipoles (magnetic or electrical) on the pyrochlore lattice has drawn considerable attention in the solid state and condensed matter communities. Akin to the triangular arrangement of points on a kagomé lattice, the cations in the pyrochlore structure comprise corner-sharing

Received: August 24, 2022
Published: November 8, 2022

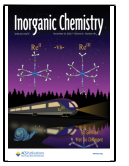

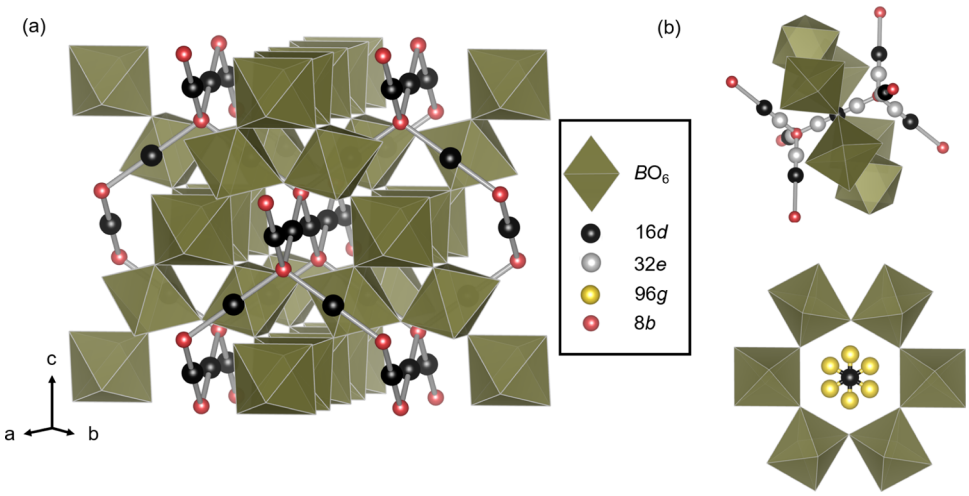

Figure 1. (a) Full $A_2B_2O_6O'$ pyrochlore structure illustrating the interpenetrated networks of A_2O' chains and BO_6 octahedra. (b) Highlight of the various atomic positions within the BO_6 channel; each color corresponds to a specific Wyckoff site (16d in black, 8b in pink, 96g in yellow, and 32e in gray).

tetrahedra with each cation on the vertices of the tetrahedra. This three-dimensional triangular arrangement leads to frustration of dipoles, as there are a number of degenerate low energy spin arrangements. This has been detailed for magnetic dipoles in the formation of spin ices[21] and the more recent proposal of the existence of magnetic monopoles,[27] and this effect can be observed with electric dipoles in the analogous charge ice.[15] Electrical dipoles are often driven by cations with electron shell configurations that contribute to off-centering within their bonding environment, particularly those with ns^2 stereochemically active lone pairs[28] or nd^0 second-order Jahn-teller (SOJT) active cations.[29] The displacement of these dipoles can be enhanced through cooperative distortions of lone pair and SOJT cations, such as in the prototypical perovskite $PbTiO_3$.[30]

While most pyrochlores display frustration of dipoles that prevents long-range ordering, a few compositions overcome this geometric constraint and exhibit polar low energy crystal structures.[3,31−36] The most prominent of these is the highly studied ferroelectric $Cd_2Nb_2O_7$.[3,37,38] The material undergoes a phase transition at approximately 204 K followed by a series of phase transitions around 196 K.[39] There are two further phase transitions reported at approximately 85 K to an uncharacterized monoclinic phase and the fourth at approximately 45 K to another unique monoclinic phase.[40−42] There is a vast amount of sometimes-conflicting literature surrounding the nature of the intermediate phases above 196 K,[40−49] while the ferroelectric phase below this temperature is reported as orthorhombic *Ima*2.[41,50] As a testament to the complexity of the interpenetrating pyrochlore networks, this structural behavior can be altered by substitution on either network (including anion substitution on the 8b Wyckoff site), and this is proposed to be due to changes in covalency of the overall system.[50] The existence of a polar phase in $Cd_2Nb_2O_7$ and the ability to alter structural behavior point to the need to further investigate the pyrochlore structure through related chemistries.

The combination of lone pair cations and vacancies in pyrochlores significantly impacts their structure and physical behavior. In $Bi_2Ti_2O_7$, there are no vacancies on the O′ site, and the material exhibits frustration and charge ice behavior at low temperatures.[15] In $Pb_2Sn_2O_6$, vacancies due to the complete absence of O′ anions result in topological frustration of the lone pair, where the lone pair cannot localize into a single lobe of electron density and instead splits into two lobes in adjacent vacancy sites for every fourth Pb atom in the structure.[15] These lone pair distortions remain frustrated, and no coherent long-range ordering is achieved. In the "ordered-ice" $Pb_2Ru_2O_6O'_{0.5}$, ordered vacancies of the O′ sites direct $6s^2$ lone pairs toward the O′, relieving geometric frustration.[51] This is reflected in heat capacity measurements, where the lattice-only contribution is significantly lower upon cooling in the ordered $Pb_2Ru_2O_6O'_{0.5}$ versus the completely disordered $Bi_2Ti_2O_7$. More broadly, Pb-based pyrochlores are a fascinating study on the stoichiometric constraints for forming the cubic $Fd\bar{3}m$ structure, as some only have vacancies on the O′ site (such as $Pb_2Sn_2O_6$ and $Pb_2Ru_2O_6O'_{0.5}$), whereas others only form the cubic structure with vacancies on both the Pb and O′ sites (such as pyrochlores $Pb_{2-x}B_2O_{7-x}$ where B = Nb, Ta, Sb[22,52,53]).

The pyrochlore $Pb_{1.5}Nb_2O_{6.5}$ presents a unique opportunity to investigate interactions between lone pairs of electrons, cations with the potential for SOJT distortions, and vacancies on both A and O′ sites. Herein, we have performed analyses of temperature-dependent neutron and X-ray total scattering data across various length scales to follow Pb and Nb displacements. We found that the ideal cubic structure describes the pyrochlore at room temperature, but short-range cristobalite-like distortions are needed to more adequately describe the structure at low temperatures. It appears that the crystallographic disorder of the lone pair distortions is directly related to the proximity of the crystallographically disordered O′ vacancies in the material. We additionally observe an emphanisis-like effect[54−56] of local symmetry breaking upon warming associated with M−O correlations, highlighting the complex behavior of lone pair expression and correlation in $Pb_{1.5}Nb_2O_{6.5}$. This behavior plays a crucial role in the structural and dielectric response of the material upon cooling, preventing a crystallographic phase transition accompanied by elevated dielectric permittivity down to the measured temperature of 100 K.

https://doi.org/10.1021/acs.inorgchem.2c03031
Inorg. Chem. 2022, 61, 18601−18610

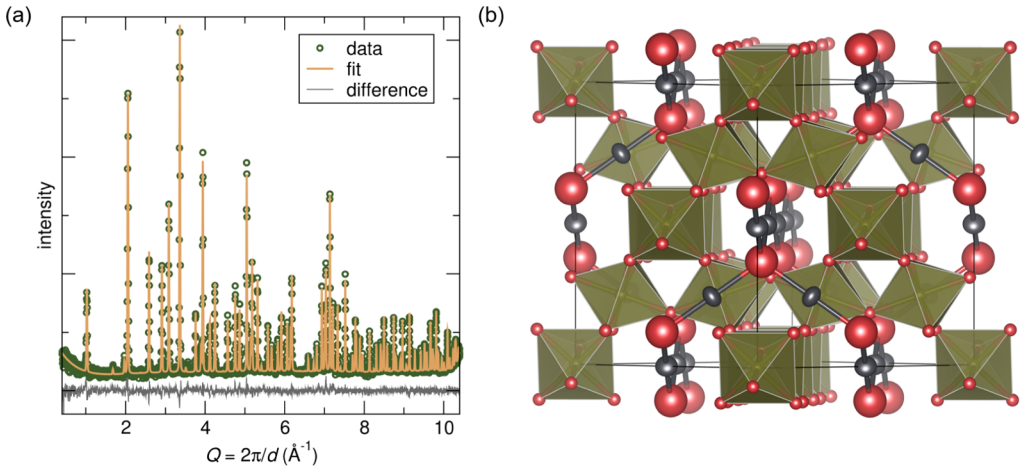

Figure 2. (a) Rietveld fit of neutron diffraction data (BT-1, NCNR, NIST) against the cubic $Fd\bar{3}m$ 16d model (resulting R_w = 7.3%). (b) Refined structure with anisotropic atomic displacement parameters (shown at 90% probability) indicates disorder on the A and O′ sites. Note that vacancies are not shown in this image and were assumed to be disordered on the A and O′ sites for the model.

METHODS

Sample Preparation. Traditional ceramic synthesis routes were utilized to synthesize a powder sample of $Pb_{1.5}Nb_2O_{6.5}$. Stoichiometric amounts of PbO (Sigma-Aldrich, 99%) and Nb_2O_5 (Alfa Aesar, 99.9985%) were ground in a mortar and pestle and then transferred into an alumina crucible. The crucible was placed inside a fused silica ampoule, which was then sealed under vacuum and heated at a rate of 10 K/min to 1273.15 K. The samples dwelled at 1273.15 K for 10 h, after which they were cooled to 298.15 K at 20 K/min. The powder products appeared yellow in color.

X-ray powder diffraction data were collected using a PANalytical Empyrean diffractometer to determine phase purity. The instrument was equipped with a PIXcel^{3D} detector and a Cu tube, operating at 45 kV and 40 mA, and a wavelength of 1.54 Å. Data were collected between the angular range of $10° \leq 2\theta \leq 90°$. Step width and step rate were 0.008° and 0.0557°/s, at room temperature, respectively. Once phase purity was determined, the sample was prepared for further measurements as described below.

The sample was prepared for dielectric measurement by placing 0.5 g of powder mixed with 1 mL of ethanol and placed in a ball-mill chamber. The sample was ball-milled for 9 h. Sample chambers were removed from the ball mill and placed in an oven at 373.15 K until the ethanol evaporated and only a dry powder sample remained. The sample was then ground with 2−3 drops of 1% polyvinyl alcohol in a mortar and pestle for 15 min and then pressed into a pellet using a hydraulic press. The pellet was placed in a new alumina crucible and then placed into a tube furnace, where it was heated to 1273.15 K with a slow ramp to remove the binding agent, resulting in a pellet with 85% theoretical density based off of refined neutron values. After sintering, silver paint was applied onto one side of the pellet. The pellet was placed in an oven at 373.15 K for 10 min to dry the silver paint. This process was repeated for the other side of the pellet, so that there was one electrode on each side. The pellet with electrodes was dried in a box furnace at 1073.15 K for 10 min.

Neutron Diffraction. Neutron scattering data were collected on the sample at room temperature from a reactor source at the NIST Center for Neutron Research. Data were measured on the BT-1 beamline in indium cans sealed under a helium atmosphere. A Ge(733) monochromator was used with a wavelength of 1.197 Å. The data were refined using the LeBail[57] and Rietveld[58] methods in the GSAS-II[59] software. The LeBail method was first performed. The background was modeled with a Chebyschev function and 12 coefficients. Histogram scale factor, unit cell parameters, and sample size were also refined. Following LeBail refinements, Rietveld refinements were performed on each data set.

Neutron total scattering data were obtained utilizing the Mantid software framework.[60,61] The pair distribution function (PDF) was generated with a Q_{max} of 31.4 Å^{-1}. The Q_{max} value was chosen to balance between resolution and termination ripples in the reduced data for each sample. Least-squares refinement of PDF data was performed using PDFGUI.[62]

Synchrotron X-ray Diffraction. Synchrotron X-ray diffraction data were obtained with λ = 0.1665 Å at the National Synchrotron Light Source II at Brookhaven National Laboratory in Upton, New York. Both X-ray powder diffraction and PDF data were collected. The data were collected on cooling, with one measurement taken per 20 K. A total of 11 measurements were taken per sample, at temperatures between 293 and 100 K. X-ray PDF data were obtained using the program PDFgetX3[63] with a Q_{max} = 22 Å^{-1}. Least-squares refinement of PDF data was performed using PDFGUI.[62]

Structural Visualization. Density functional theory (DFT) for visualization of the electron localization functions (ELFs) was performed using the Quantum Espresso software suite.[64,65] Calculations were carried out on the $P4_32_12$ cristobalite model obtained from the local fit of the neutron PDF data of $Pb_{1.5}Nb_2O_{6.5}$ at 300 K. Calculations utilized a plane wave basis set and the Perdew−Burke−Ernzerhof functional for solids (PBEsol).[66,67] Calculations were performed using a 5 × 5 × 5 Monkhorst−Pack grid for Brillouin zone sampling and Gaussian smearing for self-consistent field calculations to achieve convergence. ELFs, with an isosurface level of 0.4 e/Å^3, were used to visualize the presence of stereochemically active lone pairs in the partially occupied structures. All crystal structures were visualized using the VESTA software suite.[68]

Dielectric Characterization. Dielectric characterization was performed with in-house probes connected to a Keysight Technologies impedance analyzer. High-temperature data were obtained on heating, where the sample was placed between a parallel plate capacitor and heated, such that its capacitance was measured as a function of temperature. Samples were heated up to 423.15 K; heating was performed with an Elite Thermal Systems tube furnace, with one measurement being taken per degree increased. Similarly, low-temperature data were obtained on cooling. The sample, again placed between a parallel plate capacitor, was lowered into liquid nitrogen via a stepper motor connected to an Arduino. Capacitance values were measured as the sample was cooled to 173.15 K. For each sample, capacitance values were measured at five frequencies (1, 10, 100, 250, and 100 kHz) per scan. These capacitance values were converted to relative permittivity values factoring in sample density and dimensions and plotted as a function of temperature.

Heat Capacity. Sintered pellets of $Pb_{1.5}Nb_2O_{6.5}$ were prepared as described above. A 5.6 mg sample was used for heat capacity measurements on a Quantum Design DynaCool Physical Properties Measurement System down to T = 1.8 K. High-temperature heat

https://doi.org/10.1021/acs.inorgchem.2c03031
Inorg. Chem. 2022, 61, 18601−18610

capacity measurements (170−400 K) were additionally performed on a TA Instruments DSC 2500 using the same sample.

RESULTS

Previous reports on $Pb_{1.5}Nb_2O_{6.5}$ indicate the room-temperature structure to be cubic $Fd\bar{3}m$.[69] To verify and quantify composition, particularly oxygen content, constant wavelength neutron diffraction data were collected at room temperature at BT-1, NCNR, NIST. Neutron scattering is a useful tool to investigate relatively light elements such as oxygen within a matrix of heavy elements, for example, Pb and Nb. In addition to increased sensitivity to light atoms using neutron radiation, the use of the Ge(733) monochromator provides high full width at half-maximum resolution out to high Q, allowing more confidence in the refined oxygen-dependent parameters. The two best fits were achieved by modeling Pb either at the 16d Wyckoff position with anisotropic atomic displacement parameters (ADPs) or at the 96g site with isotropic ADPs (R_w = 7.33 and 7.28%, respectively), with the fit to the 16d model shown in Figure 2a. Vacancy disorder on the 8b site was determined for both models as fits to an O′/vacancy-ordered $F\bar{4}3m$ model (with 4a site empty and 4c site fully occupied and vice versa) resulted in R_w = 18%, significantly higher than an R_w of approximately 7% for the 16d and 96g models, indicating that the vacancies are not ordered on the 8b site. Modeling Pb at the 16d site led to enlarged U_{xx} ADP of 0.024 Å^2, indicating displacement perpendicular to the Pb−O′ bond (illustrated in Figure 2b), while modeling Pb at 96g led to a smaller U_{iso} value of 0.003 Å^2. For both models, Pb site occupancies were refined, with Pb vacancies disordered across the site. This reduction in Pb U_{isos} with off-centering suggests that the Pb atoms are statically disordered from the ideal 16d position perpendicular to the Pb−O′ bond, as has been observed for other lone-pair-bearing pyrochlores such as $Bi_2Ti_2O_7$[19] and $Bi_2Ru_2O_7$.[70] This is notably different than other Pb^{2+} pyrochlores such as $Pb_2Ru_2O_{6.5}$[51] and $Pb_2Sn_2O_6$,[15] where the Pb atoms are displaced along the Pb−O′/vacancy direction. In addition to disorder on the Pb site in $Pb_{1.5}Nb_2O_{6.5}$, a large isotropic ADP of 0.061 Å^2 on the O′ site was found regardless of model, indicating a large amount of disorder on this site. Refined isotropic ADPs of the Nb site indicate reasonable behavior of the Nb cations, with slightly elevated ADPs (0.010 Å^2). This could indicate distortion due to SOJT behavior but cannot be resolved with the Rietveld crystallographic model.

The pyrochlore structure is prone to both short-range atomic displacements and long-range correlated distortions depending on the chemistry of the composition and the nature of the distortions. Figure 3 compares two models of correlated distortions that have been observed in the literature. In the cubic $Fd\bar{3}m$ structure, the cations are found on the vertices of regular tetrahedra, displayed for the A-site sub-network in Figure 3a. The A-site atoms can displace in a 2-in-2-out fashion, resulting in an ordered $P\bar{4}3m$ model,[71,72] illustrated in Figure 3b. Alternatively, their local displacements can be characterized with a beta-cristobalite model,[17,73,74] in which the tetrahedral sub-units can rotate about the corner-shared vertices (depicted in Figure 3c,d). The cristobalite-like displacements can be described with either the $P4_32_12$ (#96) or the $P4_12_12$ (#92) space group, which are structural enantiomers and result in equivalent models for powder experiments. In the cristobalite model (either space group #96 or #92), the OPb_4 tetrahedral rotations break the planar symmetry of the ideal ring of OPb_4 tetrahedra in the $Fd\bar{3}m$

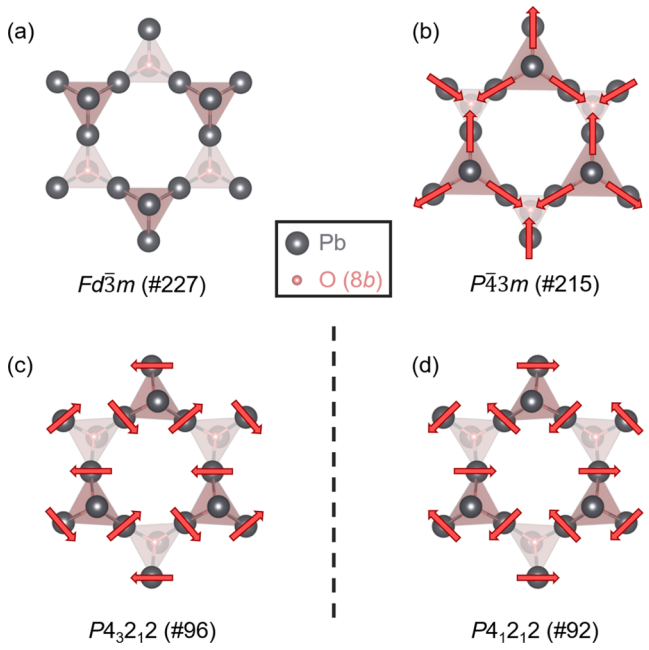

Figure 3. Illustration of Pb distortions in the local models used for analysis of PDF data: (a) cubic $Fd\bar{3}m$ with no OPb_4 distortions; (b) cubic $P\bar{4}3m$ model with "two in two out" distortions of Pb; (c,d) cristobalite-type distortions, shown here as the two enantiomorphic space groups with rotations of the OPb_4 tetrahedra.

model. These established structural displacements, along with our observations of enlarged ADPs on the Pb and O′ site, led us to perform variable temperature neutron total scattering experiments at NOMAD to further investigate the nature of the disorder across various length scales in $Pb_{1.5}Nb_2O_{6.5}$.

Rietveld analyses of variable temperature neutron powder diffraction data (NOMAD, SNS, ORNL) indicate that an $Fd\bar{3}m$ model (either 16d or 96g variations) accurately describes the average structure at room temperature down to 100 K, with R_w values less than 10% for all temperatures (fits shown in Supporting Information, Figure S1). The refinements indicate an increase in R_w with cooling, accompanied by elevated ADPs for Pb and O′ at all temperatures. The Nb U_{iso} values decrease slightly upon cooling. This suggests that the off-centering is static, and disorder on Pb and O′ sites persists at all measured temperatures. A summary of the Rietveld refinements can be found in the Supporting Information, Table S1.

To investigate the nature of the disorder on the Pb and O′ sites, joint analysis of the neutron (NOMAD, SNS, ORNL) and X-ray (PDF, NSLS-II, BNL) PDF was performed at 300, 200, and 100 K. The data were fit against various structural models over different real-space ranges in order to determine the best structural descriptor of the data over a given length scale. For example, the local structure is fit from 1.6−6 Å, which captures the coordination environments of the Nb and Pb cations as well as intraoctahedral interactions such as Nb−Nb and O−O. The partial contributions to the PDF can be found in the Supporting Information, Figure S2. Structural candidates were compared and evaluated by the goodness-of-fit metric R_w and by observations of the fits of specific peaks in the data informed by the partial PDFs.

The data was initially fit against the two $Fd\bar{3}m$ models, and the fits to the data for the 16d and 96g models can be seen in the Supporting Information, Figures S3 and S4, respectively.

https://doi.org/10.1021/acs.inorgchem.2c03031
Inorg. Chem. 2022, 61, 18601−18610

The data are well-described by the models over the long range (r > 6 Å), but it can be observed that the peaks are not completely described in the local range (r < 6 Å), indicated by dashed lines in the fits. This suggests that the local arrangements of atoms is lower in symmetry than $Fd\bar{3}m$ and prompts investigation using the distorted $P\bar{4}3m$ and cristobalite models.

The R_w values of the fits against the four candidate models—$Fd\bar{3}m$ (Pb in 16d), $Fd\bar{3}m$ (Pb in 96g), $P\bar{4}3m$, and $P4_32_12$/$P4_12_12$ cristobalite—across different real-space distances (upper bound of fit indicated by r_{max}) are shown in Figure 4.

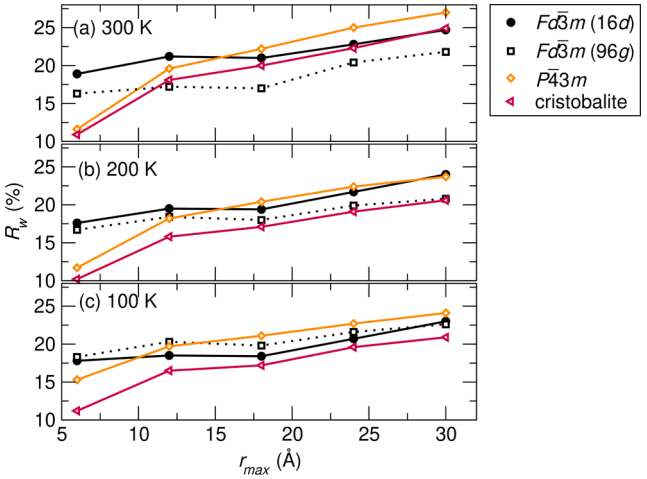

Figure 4. Goodness-of-fit parameter R_w of the various local models fit against joint NPDF (NOMAD, SNS) and XPDF (28-ID-1, BNL) data as a function of r-range at (a) 300, (b) 200, and (c) 100 K. The most local fit (r = 1.6−6 Å) is best described with the lowest R_w by the cristobalite model at all temperatures as well as intermediate (r = 1.6−12, 18 Å) and long range (r = 1.6−24, 30 Å) at lower temperatures, whereas the lowest R_w is observed for the cubic $Fd\bar{3}m$ (96g) model with the intermediate and long-range data at 300 K.

At all temperatures, the local structure (fits up to 6 Å) is best described by the cristobalite model. At 300 K, this distortion is only observed locally, as cubic $Fd\bar{3}m$ structure is the best description of the data at and greater than r_{max} of 12 Å. Upon cooling, the cristobalite structure appears to equally or better describe the data out to longer length scales (r_{max} of 30 Å). The R_w of the fit against the cristobalite model data is the lowest for all length scales at 100 K, suggesting a long-range structural transition upon cooling.

To investigate the presence of a phase transition upon cooling, the reciprocal space neutron diffraction data (NOMAD, SNS, ORNL) was fit against the cristobalite models obtained from the 30 Å fits at 300, 200, and 100 K. Compared to the $Fd\bar{3}m$ model, the cristobalite model yielded a higher R_w at room temperature (5.5% for cubic vs 10.2% for cristobalite). Fits with the cristobalite model improved with lower temperature but were not statistically significant enough to suggest a long-range phase transition (6.2% for cubic vs 9.1% for cristobalite at 100 K).

To further investigate the existence of structural transitions upon cooling and the structural influence on physical properties, heat capacity and dielectric permittivity measurements were performed on the samples. The dielectric permittivity at room temperature is in agreement with previous literature on lead niobates[52] and indicates a feature at approximately 220 K, shown in Figure 5a, which is

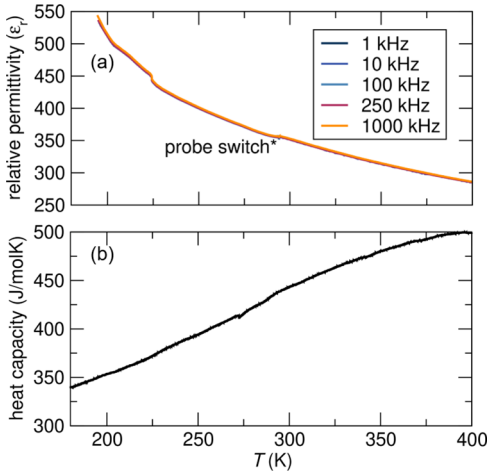

Figure 5. (a) Dielectric permittivity as a function of temperature at various frequencies; (b) heat capacity as a function of temperature measured by differential scanning calorimetry. * indicates where the data was connected, collected by separate low temperature and high temperature probes.

reproducible with other samples of the same composition. A relatively high and consistent dielectric permittivity is observed across the measured range, accompanied by low loss (tanδ less than 0.01). The shape of the 220 K feature does not indicate a ferroelectric phase transition—which would be indicated by a peak in the dielectric data at a transition temperature—it does suggest that there may be a structural change at this temperature, which is consistent with observations of a cristobalite-type distortion persisting at longer length scales upon cooling.

The heat capacity measurements were performed through differential scanning calorimetry (DSC, Figure 5b) and using a physical properties measurement system (PPMS) to investigate behavior at lower temperatures. Heat capacity measurements do not indicate any apparent long-range phase transitions in the sample upon cooling, which supports $Fd\bar{3}m$ as the best structural description of the diffraction data at all temperatures.

DISCUSSION

Of the candidate distortion models considered, the cristobalite-type distortion better describes the M−O bond lengths (compared to the $Fd\bar{3}m$ structure, illustrated in Figure 6) by capturing the metal coordination environments more successfully. The areas of the PDFs that are most improved with the cristobalite model are the Pb-dependent correlations, and while the distorted model may be a better description of the Nb−O peaks (indicating SOJT activity), it is difficult to assess given the overlap with the broadened Pb−O peaks. An element-specific local probe such as solid-state NMR or X-ray absorption is needed to investigate distortions in the Nb coordination environment. In addition to the coordination environments, the peaks between 4 and 4.5 Å are better captured with this cristobalite model. The partial PDFs from the high symmetry $Fd\bar{3}m$ are plotted in Figure S2, and it can be seen that the peaks between 4 and 4.5 Å are primarily the first M−M interaction as well as O−O correlations, indicating that the cristobalite structure is the best description of the interactions between neighboring tetrahedral sub-units. In addition to these local structural interactions, the cubic $Fd\bar{3}m$

https://doi.org/10.1021/acs.inorgchem.2c03031
Inorg. Chem. 2022, 61, 18601−18610

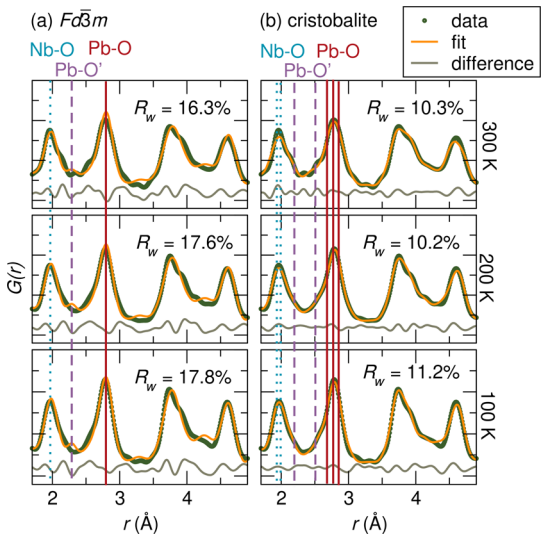

Figure 6. Local fits of the NPDF data (NOMAD, SNS) as a function of temperature against the (a) cubic $Fd\bar{3}m$ model and the (b) cristobalite model indicates that a better fit is obtained at all temperatures with the cristobalite-type distortion. Dashed lines indicate M−O bond lengths, which are still not well described at room temperature, indicating a further distortion of the local structure upon warming.

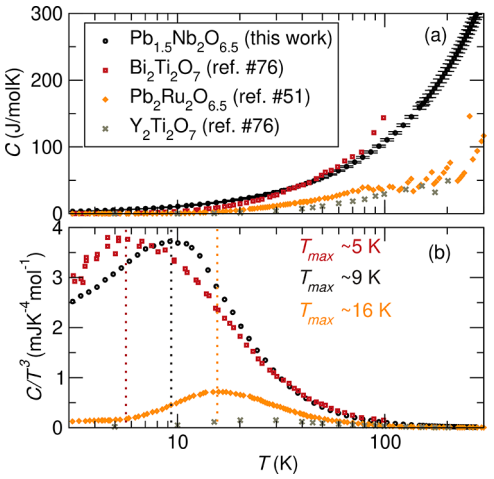

Figure 7. (a) Specific heat (C) and (b) C/T^3 vs T of $Pb_{1.5}Nb_2O_{6.5}$ (black) compared with data from the literature on other pyrochlores (error bars represent one σ). $Y_2Ti_2O_7$ (gray) exhibits the least amount of disorder and Debye-like behavior (data from ref 76). $Pb_2Ru_2O_{6.5}$ (yellow) has a small degree of disorder due to stereochemically active lone pairs (data from ref 51), but the correlated ordering of these distortions results in a much more ordered structure than the charge ice $Bi_2Ti_2O_7$ (red), which has the highest amount of disorder of the samples (data from ref 76).

models show poorer fits to the data up to approximately 13 Å (approximately the distance of the diagonal of the face of one unit cell), but the difference curves shown in Figures S3 and S4 fits show a qualitatively better fit to the cubic model at all temperatures past 13 Å up to 30 Å. This supports our observations through Rietveld and calorimetric analyses that the material does not undergo a clear phase transition but suggests that the global structure, while cubic, might be better described as a somewhat disordered version of the cristobalite structure that averages out to appear cubic.

It is well understood that the low-temperature specific heats of highly disordered materials such as glasses and other amorphous systems illustrate deviation from the Debye model,[75] which estimates the phonon contribution to the specific heat in a solid material. The observed excess specific heat arises from low energy vibrational modes that are not captured by the Debye model and is observed as a peak in a plot of C/T^3 as a function of temperature. This deviation from Debye behavior has been observed in pyrochlores that exhibit charge ice frustration of lone pair-bearing cations, with the temperature of the peak maxima occurring at lower temperatures (and higher C/T^3) the more disordered the structure. Figure 7 illustrates our data presented in context with data from other pyrochlores in the literature. $Y_2Ti_2O_7$ serves as a good reference pyrochlore for Debye behavior,[76] as it lacks lone pair cations and its low temperature heat capacity can be predicted by the Debye model. Contrary to $Y_2Ti_2O_7$, the charge-ice $Bi_2Ti_2O_7$ is documented to have a high degree of disorder due to the stereochemically active lone pair cation Bi^{3+}.[76] It can be observed that the data for $Bi_2Ti_2O_7$ peaks at the lowest temperature and has the highest value at its peak, a result of the highly disordered lone pairs. While $Pb_2Ru_2O_{6.5}$ also has lone pairs associated with its A-site cation, the presence of ordered O′ vacancies allows the lone pair distortions to order, resulting in a higher temperature and lower value of the peak maximum.[51] It should be noted that even though these lone pairs are ordered, they still contribute to the phonon behavior in excess of the Debye model. Our $Pb_{1.5}Nb_2O_{6.5}$ measurements exhibit temperature and peak maximum values closer to that of $Bi_2Ti_2O_7$, which is in agreement with disordered vacancies and lone pair-driven distortions in the material.

The existence and ordering of the O′ vacancies in $Pb_2Ru_2O_{6.5}$ are consequential on the ordering of lone pair-driven distortions in the material. To understand the interplay between vacancy and lone pair distortions in $Pb_{1.5}Nb_2O_{6.5}$, DFT calculations were performed on the distorted cristobalite model to understand the nature of the stereochemically active lone pair. ELF reveal that lone pair density forms on Pb sites which are undercoordinated by O′ and directly adjacent to a vacancy. However, lone pair density is not apparent on Pb sites which are fully coordinated by O′ species, and the electron density around the Pb atom is spherical and more s-like in nature. Such behavior is demonstrated in Figure 8, where

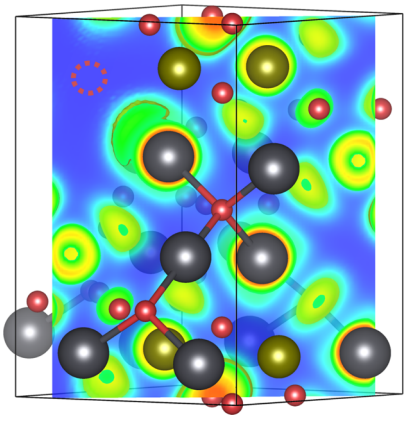

Figure 8. ELF of the distorted cristobalite structure shown along a (110) slice of the unit cell with an isosurface level set to 0.4 e/Å^3. The location of an O′ vacancy is indicated by the red dashed circle.

https://doi.org/10.1021/acs.inorgchem.2c03031
Inorg. Chem. 2022, 61, 18601−18610

localized lone pair density is present on the undercoordinated Pb site next to a vacancy (indicated by a dashed circle) and faces toward the vacant O′ site. This suggests that a lone pair-driven distortion only occurs when a Pb cation is near a vacancy. This is similar to conclusions about the role of vacancies in the formation of dipoles in $Pb_2Ru_2O_{6.5}$,[51] where ordering of these vacancies is tied to the ordering of the lone pair distortions. In $Pb_{1.5}Nb_2O_{6.5}$, the vacancies are not ordered, and thus, any lone pair-driven dipoles are spatially disordered, preventing any global phase transition and giving rise to the observed low temperature structural and heat capacity behavior. This work additionally poses the question of chemical considerations and vacancy formation in the cubic $Fd\bar{3}m$ structure. A limited number of Pb-based pyrochlores form the cubic structure with vacancies on both A and O′ sites. Such pyrochlores, including $Pb_{1.5}Nb_2O_{6.5}$[52] and $Pb_{1.5}Ta_2O_{6.5}$,[53] possess relatively electropositive B-site cations with a 5+ oxidation state. Other Pb-based cubic pyrochlores, such as $Pb_2Tc_2O_{7-x}$,[77] $Pb_2Ru_2O_{6.5}$,[51] $Pb_2Rh_2O_{7-x}$,[78] $Pb_2Re_2O_{7-x}$,[79] $Pb_2Os_2O_{7-x}$,[80] and $Pb_2Ir_2O_{6.5}$,[81] possess more electronegative B-site cations with mixed-valent 4+/5+ oxidation states and exhibit vacancies on the O′ site. When the B-site cation only exhibits a 4+ oxidation state (such as in $Pb_2Sn_2O_6$[15]), the A-site is fully occupied and the O′ site is vacant to maintain charge neutrality. This suggests that the identity and chemistry of the B-site cation is a critical component in the formation of vacancies (and by extension lone pair behavior) in Pb-pyrochlores. A detailed DFT study of the relationship between vacancy formation, ordering schemes, proximity to Pb (and Pb vacancies), and consequent lone pair expression in the high symmetry $Fd\bar{3}m$ phase of $Pb_{1.5}Nb_2O_{6.5}$ is the subject of a forthcoming article.

CONCLUSIONS

It is evident through this work that the lone pair behavior of $Pb_{1.5}Nb_2O_{6.5}$ is complex and directly tied to the nature of the vacancies on the O′ site of the pyrochlore network. Both vacancies and lone pair-driven distortions of the Pb cations are globally disordered in the cubic $Fd\bar{3}m$ structure, and local analysis reveals that these distortions can be described by the cristobalite structure. This cristobalite distortion persists to longer length scales upon cooling, and at low temperatures, it is suggested that the global structure may be more accurately described as a disordered cristobalite-type structure. Interestingly, closer inspection of the variable temperature data (displayed together in the Supporting Information, Figure S5) reveals the appearance of shoulders on the peaks that correspond to the Pb−O′ bond distances in the pyrochlore structure. This apparent lowering of the local symmetry at high temperatures is similar to the observation of emphanisis in lone pair containing materials PbTe,[54] SnTe,[55] and $CsSnBr_3$,[56] suggesting that there may be multiple effects of the lone pair cation on the resulting structural behavior. This work reiterates the impact of vacancies on lone pair expression in Pb pyrochlores and demonstrates that controlling the ordering of vacancies is critical to long-range correlations of lone pair distortions on the pyrochlore network, which in turn are critical to driving properties, such as the sustained elevated dielectric behavior shown herein.

ASSOCIATED CONTENT

Supporting Information

The Supporting Information is available free of charge at https://pubs.acs.org/doi/10.1021/acs.inorgchem.2c03031.

Refined crystallographic data for the nominal $Pb_{1.5}Nb_2O_{6.5}$ with the A-site cation in the ideal 16d position; fits of the neutron diffraction data at 300, 200, and 100 K against the $Fd\bar{3}m$ model with Pb in the 16d Wyckoff position; experimental data collected at various temperatures compared to calculated partials from cubic $Fd\bar{3}m$ model with the A-site cation in the 16d Wyckoff position; fits of the NPDF data against the cubic $Fd\bar{3}m$ model at 300, 200, and 100 K; fits of the NPDF data against the cubic $Fd\bar{3}m$ model at 300, 200, and 100 K; and variable temperature neutron (NOMAD, SNS) and X-ray (28-ID-1, BNL) PDF data from 300 to 100 K (PDF)

AUTHOR INFORMATION

Corresponding Authors

Geneva Laurita − *Department of Chemistry and Biochemistry, Bates College, Lewiston, Maine 04240, United States;* orcid.org/0000-0001-9577-150X; Email: glaurita@bates.edu

Robin T. Macaluso − *Department of Chemistry and Biochemistry, University of Texas at Arlington, Arlington, Texas 76019, United States;* orcid.org/0000-0002-0021-0775; Email: robin.macaluso@uta.edu

Authors

Uyen Dang − *Department of Chemistry and Biochemistry, University of Texas at Arlington, Arlington, Texas 76019, United States*

Jake O'Hara − *Department of Chemistry and Biochemistry, Bates College, Lewiston, Maine 04240, United States;* orcid.org/0000-0002-5061-1681

Hayden A. Evans − *Center for Neutron Research, National Institute of Standards and Technology, Gaithersburg, Maryland 20899, United States;* orcid.org/0000-0002-1331-4274

Daniel Olds − *National Synchrotron Light Source-II, Brookhaven National Laboratory, Upton, New York 19973, United States*

Juan Chamorro − *Materials Department, University of California, Santa Barbara, California 93106, United States*

Daniel Hickox-Young − *Department of Mathematics, Computer Science and Physics, Roanoke College, Salem, Virginia 24153, United States;* orcid.org/0000-0002-5411-0497

Complete contact information is available at: https://pubs.acs.org/10.1021/acs.inorgchem.2c03031

Notes

The authors declare no competing financial interest.

ACKNOWLEDGMENTS

J.O. and G.L. were supported by Bates College internal funding and the National Science Foundation (NSF) through DMR 1904980. Work by U.D. and R.T.M. was supported by the NSF under DMR 2113689. We acknowledge the support of the National Institute of Standards and Technology, U.S. Department of Commerce, in providing the neutron research facilities

used in this work. Neutron diffraction data were collected at the National Institute of Standards and Technology Center for Neutron Research (NCNR). This research used resources at the Spallation Neutron Source, a DOE Office of Science User Facility operated by the Oak Ridge National Laboratory, and the authors thank Michelle Everett for assistance with data acquisition. This research used the pair distribution function (PDF) beamline of the National Synchrotron Light Source II, a U.S. Department of Energy (DOE) Office of Science User Facility operated for the DOE Office of Science by Brookhaven National Laboratory under Contract no. DE-SC0012704. Computations were performed on the Bates High Performance Computing Center's *Leavitt* system. J.O. would like to thank Professor Jeff Oishi for his guidance in using the *Leavitt* HPC cluster at Bates College. G.L. additionally thanks Ram Seshadri for insightful discussions. Certain commercial equipment, instruments, or materials are identified in this document. Such identification does not imply recommendation or endorsement by the National Institute of Standards and Technology, nor does it imply that the products identified are necessarily the best available for the purpose.

REFERENCES

(1) Converse, E. S.; Li, J.; Haskel, D.; LaBarre, P. G.; Ramirez, A. P.; Subramanian, M. A. Os4+ Instability in the Pyrochlore Structure: Tl2−xBixOs2O7−y. *Inorg. Chem.* **2020**, *59*, 1227−1233.

(2) Deng, Z. Q.; Niu, H. J.; Kuang, X. J.; Allix, M.; Claridge, J. B.; Rosseinsky, M. J. Highly Conducting Redox Stable Pyrochlore Oxides. *Chem. Mater.* **2008**, *20*, 6911−6916.

(3) Cook, W. R.; Jaffe, H. Ferroelectricity in Oxides of Fluorite Structure. *Phys. Rev.* **1953**, *89*, 1297−1298.

(4) Kako, T.; Kikugawa, N.; Ye, J. Photocatalytic activities of $AgSbO_3$ under visible light irradiation. *Catal. Today* **2008**, *131*, 197−202 , Recent advances in catalysis—selected papers from APCAT 4 (Singapore, 6-8 December 2006).

(5) Uma, S.; Singh, J.; Thakral, V. Facile Room Temperature Ion-Exchange Synthesis of Sn2+ Incorporated Pyrochlore-Type Oxides and Their Photocatalytic Activities. *Inorg. Chem.* **2009**, *48*, 11624−11630.

(6) Reimers, J.; Greedan, J.; Sato, M. The crystal structure of the spin-glass pyrochlore, $Y_2Mo_2O_7$. *J. Solid State Chem.* **1988**, *72*, 390−394.

(7) Yang, J.; Dai, J.; Liu, Z.; Yu, R.; Hojo, H.; Hu, Z.; Pi, T.; Soo, Y.; Jin, C.; Azuma, M.; Long, Y. High-Pressure Synthesis of the Cobalt Pyrochlore Oxide Pb2Co2O7 with Large Cation Mixed Occupancy. *Inorg. Chem.* **2017**, *56*, 11676−11680.

(8) Babu, G. S.; Valant, M.; Page, K.; Llobet, A.; Kolodiazhnyi, T.; Axelsson, A.-K. New (Bi1.88Fe0.12)(Fe1.42Te0.58)O6.87 Pyrochlore with Spin-Glass Transition. *Chem. Mater.* **2011**, *23*, 2619−2625.

(9) Pomjakushina, E.; Pomjakushin, V.; Rolfs, K.; Karpinski, J.; Conder, K. New Synthesis Route and Magnetic Structure of Tm2Mn2O7 Pyrochlore. *Inorg. Chem.* **2015**, *54*, 9092−9097.

(10) Fujihara, S.; Tokumo, K. Multiband Orange-Red Luminescence of Eu3+ Ions Based on the Pyrochlore-Structured Host Crystal. *Chem. Mater.* **2005**, *17*, 5587−5593.

(11) Burggraaf, A.; van Dijk, T.; Verkerk, M. Structure and conductivity of pyrochlore and fluorite type solid solutions. *Solid State Ionics* **1981**, *5*, 519−522 , Proceedings of the International Conference on Fast Ionic Transport in Solids.

(12) Pandey, J.; Shrivastava, V.; Nagarajan, R. Metastable Bi2Zr2O7 with Pyrochlore-like Structure: Stabilization, Oxygen Ion Conductivity, and Catalytic Properties. *Inorg. Chem.* **2018**, *57*, 13667−13678.

(13) Radhakrishnan, A. N.; Prabhakar Rao, P.; Mahesh, S. K.; Vaisakhan Thampi, D. S.; Koshy, P. Role of Bond Strength on the Lattice Thermal Expansion and Oxide Ion Conductivity in Quaternary Pyrochlore Solid Solutions. *Inorg. Chem.* **2012**, *51*, 2409−2419.

(14) Marlton, F. P.; Zhang, Z.; Zhang, Y.; Proffen, T. E.; Ling, C. D.; Kennedy, B. J. Lattice Disorder and Oxygen Migration Pathways in Pyrochlore and Defect-Fluorite Oxides. *Chem. Mater.* **2021**, *33*, 1407−1415.

(15) Seshadri, R. Lone pairs in insulating pyrochlores: Ice rules and high-k behavior. *Solid State Sci.* **2006**, *8*, 259−266.

(16) Fennie, C. J.; Seshadri, R.; Rabe, K. M. Lattice instabilities in cubic pyrochlore Bi2Ti2O7. arXiv:0712.1846, **2007**.

(17) Shoemaker, D. P.; Seshadri, R.; Hector, A. L.; Llobet, A.; Proffen, T.; Fennie, C. J. Atomic displacements in the charge ice pyrochlore $Bi_2Ti_2O_6O'$ studied by neutron total scattering. *Phys. Rev. B* **2010**, *81*, 144113.

(18) Esquivel-Elizondo, J. R.; Hinojosa, B. B.; Nino, J. C. $Bi_2Ti_2O_7$: It Is Not What You Have Read. *Chem. Mater.* **2011**, *23*, 4965−4974.

(19) Hector, A. L.; Wiggin, S. B. Synthesis and structural study of stoichiometric $Bi_2Ti_2O_7$ pyrochlore. *J. Solid State Chem.* **2004**, *177*, 139−145.

(20) Oka, K.; Hojo, H.; Azuma, M.; Oh-ishi, K. Temperature-Independent, Large Dielectric Constant Induced by Vacancy and Partial Anion Order in the Oxyfluoride Pyrochlore $Pb_2Ti_2O_{2-\delta}F_{2\delta}$. *Chem. Mater.* **2016**, *28*, 5554−5559.

(21) Gardner, J. S.; Gingras, M. J. P.; Greedan, J. E. Magnetic pyrochlore oxides. *Rev. Mod. Phys.* **2010**, *82*, 53−107.

(22) Subramanian, M.; Aravamudan, G.; Subba Rao, G. S. Oxide pyrochlores - A review. *Prog. Solid State Chem.* **1983**, *15*, 55−143.

(23) Radosavljevic, I.; Evans, J.; Sleight, A. Synthesis and Structure of Pyrochlore-Type Bismuth Titanate. *J. Solid State Chem.* **1998**, *136*, 63−66.

(24) Avdeev, M.; Haas, M.; Jorgensen, J.; Cava, R. Static disorder from lone-pair electrons in $Bi_{2-x}M_xRu_2O_{7y}$(M=Cu,Co;x=0,0.4) pyrochlores. *J. Solid State Chem.* **2002**, *169*, 24−34.

(25) Levin, I.; Amos, T.; Nino, J.; Vanderah, T.; Randall, C.; Lanagan, M. Structural Study of an Unusual Cubic Pyrochlore $Bi_{1.5}Zn_{0.92}Nb_{1.5}O_{6.92}$. *J. Solid State Chem.* **2002**, *168*, 69−75.

(26) Laurita, G.; Page, K.; Sleight, A. W.; Subramanian, M. A. Structural Investigation of the Substituted Pyrochlore AgSbO3 through Total Scattering Techniques. *Inorg. Chem.* **2013**, *52*, 11530.

(27) Khomskii, D. Electric dipoles on magnetic monopoles in spin ice. *Nat. Commun.* **2012**, *3*, 904.

(28) Laurita, G.; Seshadri, R. Chemistry, Structure, and Function of Lone Pairs in Extended Solids. *Acc. Chem. Res.* **2022**, *55*, 1004−1014.

(29) Halasyamani, P. S. Asymmetric Cation Coordination in Oxide Materials: Influence of Lone-Pair Cations on the Intra-octahedral Distortion in d0 Transition Metals. *Chem. Mater.* **2004**, *16*, 3586−3592.

(30) Megaw, H. *Ferroelectricity in Crystals*; Methuen: London, 1957.

(31) Bernard, D.; Lucas, J.; Rivoallan, L. Les Pyrochlores Ferroelectriques Derives de $Cd_2Nb_2O_6S$: Mise en Evidence des Transistions de Phase par des Techniques D'optique Non Lineare. *Solid State Commun.* **1976**, *18*, 927−930.

(32) Dong, X. W.; Wang, K. F.; Luo, S. J.; Wan, J. G.; Liu, J. M. Coexistence of Magnetic and Ferroelectric Behaviors of Pyrochlore $Ho_2Ti_2O_7$. *J. Appl. Phys.* **2009**, *106*, 104101.

(33) Liu, D.; Lin, L.; Liu, M. F.; Yan, Z. B.; Dong, S.; Liu, J.-M. Multiferroicity in Spin Ice $Ho_2Ti_2O_7$: An Investigation on Single Crystals. *J. Appl. Phys.* **2013**, *113*, 17D901.

(34) Saitzek, S.; Shao, Z.; Bayart, A.; Ferri, A.; Huvé, M.; Roussel, P.; Desfeux, R. Ferroelectricity in $La_2Zr_2O_7$ Thin Films with a Frustrated Pyrochlore-Type Structure. *J. Mater. Chem. C* **2014**, *2*, 4037.

(35) Kimura, M.; Nanamatsu, S.; Kawamura, T.; Matsushita, S. Ferroelectric, Electro-optic and Piezoelectric Properties of $Nd_2Ti_2O_7$ Single Crystal. *Jpn. J. Appl. Phys.* **1974**, *13*, 1473−1474.

(36) McQueen, T. M.; West, D. V.; Muegge, B.; Huang, Q.; Noble, K.; Zandbergen, H. W.; Cava, R. J. Frustrated Ferroelectricity in Niobate Pyrochlores. *J. Phys. Condens. Matter* **2008**, *20*, 235210.

https://doi.org/10.1021/acs.inorgchem.2c03031
Inorg. Chem. 2022, 61, 18601−18610

(37) Shirane, G.; Pepinsky, R. Dielectric, X-Ray, and Optical Study of Ferroelectric $Cd_2Nb_2O_7$ and Related Compounds. *Phys. Rev.* **1953**, *92*, 504.
(38) Jona, F.; Shirane, G.; Pepinsky, R. Dielectric, X-Ray, and Optical Study of Ferroelectric $Cd_2Nb_2O_7$ and Related Compounds. *Phys. Rev.* **1955**, *98*, 903−909.
(39) Tachibana, M.; Kawaji, H.; Atake, T. Calorimetric Investigation of Successive Phase Transitions in $Cd_2Nb_2O_7$. *Phys. Rev. B* **2004**, *70*, 064103.
(40) Fischer, M.; Malcherek, T.; Bismayer, U.; Blaha, P.; Schwarz, K. Structure and Stability of $Cd_2Nb_2O_7$ and $Cd_2Ta_2O_7$ Explored by Ab Initio Calculations. *Phys. Rev. B* **2008**, *78*, 014108.
(41) Malcherek, T.; Bismayer, U.; Paulmann, C. The Crystal Structure of $Cd_2Nb_2O_7$): Symmetry Mode Analysis of the Ferroelectric Phase. *J. Phys. Condens. Matter* **2010**, *22*, 205401.
(42) Tachibana, M.; Fritsch, K.; Gaulin, B. D. X-ray Scattering Studies of Structural Phase Transitions in Pyrochlore $Cd_2Nb_2O_7$. *J. Phys. Condens. Matter* **2013**, *25*, 435902.
(43) Smolenskii, G. A.; Salaev, F. M.; Kamzina, L. S.; Krainik, N. N.; Dorogovtsev, S. N. The Investigation of Successive Phase Transitions in Cadmium Pyroniobate Crystal. *Sov. Tech. Phys. Lett.* **1983**, *10*, 253.
(44) Smolenskii, G. A.; Krainik, N. N.; Trepakov, V. A.; Babinsky, A. V. Photoluminescence and Carrier Drift Mobility at the Ferroelectric Phase Transitions. *Ferroelectrics* **2011**, *26*, 835−838.
(45) Lukaszewicz, K.; Pietraszko, A.; Stepie-Damm, J.; Kolpakova, N. Temperature Dependence of the Crystal Structure and Dynamic Disorder of Cadmium in Cadmium Pyroniobates $Cd_2Nb_2O_7$ and $Cd_2Ta_2O_7$. *Mater. Res. Bull.* **1994**, *29*, 987−992.
(46) Kolpakova, N. N.; Waplak, S.; Bednarski, W. EPR Spectroscopy and Optical Microscopy Study of Ferroic States in Pyrochlore. *J. Phys. Condens. Matter* **1998**, *10*, 9309−9316.
(47) Buixaderas, E.; Kamba, S.; Petzelt, J.; Savinov, M.; Kolpakova, N. N. Phase Transitions Sequence in Pyrochlore $Cd_2Nb_2O_7$ Studied by IR Reflectivity. *Phase Transitions* **2001**, *19*, 9−16.
(48) Kolpakova, N. N.; Syrnikov, P. P.; Lebedev, A. O.; Czarnecki, P.; Nawrocik, W.; Perrot, C.; Szczepanska, L. 2-5 Pyrochlore Relaxor Ferroelectric $Cd_2Nb_2O_7$ and its Fe^{2+}/Fe^{3+} Modifications. *J. Appl. Phys.* **2001**, *90*, 6332−6340.
(49) Ye, Z. G.; Kolpakova, N. N.; Rivera, J.-P.; Schmid, H. Optical and Electric Investigations of the Phase Transitions in Pyrochlore $Cd_2Nb_2O_7$. *Ferroelectrics* **1991**, *124*, 275−280.
(50) Laurita, G.; Hickox-Young, D.; Husremovic, S.; Li, J.; Sleight, A. W.; Macaluso, R.; Rondinelli, J. M.; Subramanian, M. A. Covalency-driven Structural Evolution in the Polar Pyrochlore Series Cd2Nb2O7−x S x. *Chem. Mater.* **2019**, *31*, 7626−7637.
(51) Shoemaker, D. P.; Llobet, A.; Tachibana, M.; Seshadri, R. Reverse Monte Carlo neutron scattering study of the 'ordered-ice' oxide pyrochlore $Pb_2Ru_2O_{6.5}$. *J. Phys.: Condens. Matter* **2011**, *23*, 315404.
(52) Ubic, R.; Reaney, I. M. Structure and Dielectric Properties of Lead Pyrochlores. *J. Am. Ceram. Soc.* **2002**, *85*, 2472−2478.
(53) Menguy, N.; Thuriès, F.; Caranoni, C. Stoichiometry, Defects, and Ordering in Lead Tantalum Oxides with Pyrochlore-Related Structures. *J. Solid State Chem.* **1996**, *126*, 253−260.
(54) Božin, E. S.; Malliakas, C. D.; Souvatzis, P.; Proffen, T.; Spaldin, N. A.; Kanatzidis, M. G.; Billinge, S. J. L. Entropically Stabilized Local Dipole Formation in Lead Chalcogenides. *Science* **2010**, *330*, 1660−1663.
(55) Knox, K. R.; Bozin, E. S.; Malliakas, C. D.; Kanatzidis, M. G.; Billinge, S. J. L. Local Off-Centering Symmetry Breaking in the High-Temperature Regime of SnTe. *Phys. Rev. B: Condens. Matter Mater. Phys.* **2014**, *89*, 014102.
(56) Fabini, D. H.; Laurita, G.; Bechtel, J. S.; Stoumpos, C. C.; Evans, H. A.; Kontos, A. G.; Raptis, Y. S.; Falaras, P.; Van der Ven, A.; Kanatzidis, M. G.; Seshadri, R. Dynamic Stereochemical Activity of the Sn^{2+} Lone Pair in Perovskite $CsSnBr_3$. *J. Am. Chem. Soc.* **2016**, *138*, 11820−11832.
(57) Le Bail, A. Whole Powder Pattern Decomposition Methods and Applications: A Retrospection. *Powder Diffr.* **2005**, *20*, 316−326.
(58) Rietveld, H. M. A Profile Refinement Method for Nuclear and Magnetic Structures. *J. Appl. Crystallogr.* **1969**, *2*, 65−71.
(59) Toby, B. H.; Von Dreele, R. B. GSAS-II: the genesis of a modern open-source all purpose crystallography software package. *J. Appl. Crystallogr.* **2013**, *46*, 544−549.
(60) Arnold, O.; et al. Mantid−Data analysis and visualization package for neutron scattering and μ SR experiments. *Nucl. Instrum. Methods Phys. Res. Sect. A Accel. Spectrom. Detect. Assoc. Equip.* **2014**, *764*, 156−166.
(61) Olds, D.; Saunders, C. N.; Peters, M.; Proffen, T.; Neuefeind, J.; Page, K. Precise implications for real-space pair distribution function modeling of effects intrinsic to modern time-of-flight neutron diffractometers. *Acta Crystallogr., Sect. A: Found. Adv.* **2018**, *74*, 293−307.
(62) Farrow, C. L.; Juhas, P.; Liu, J. W.; Bryndin, D. B.; Božin, E. S. J.; Bloch, T.; Proffen, S. J. L.; Billinge, S. J. L. PDFfit2 and PDFgui: computer programs for studying nanostructure in crystals. *J. Phys.: Condens. Matter* **2007**, *19*, 335219.
(63) Juhás, P.; Davis, T.; Farrow, C. L.; Billinge, S. J. L. PDFgetX3: a rapid and highly automatable program for processing powder diffraction data into total scattering pair distribution functions. *J. Appl. Crystallogr.* **2013**, *46*, 560−566.
(64) Giannozzi, P.; Baseggio, O.; Bonfà, P.; Brunato, D.; Car, R.; Carnimeo, I.; Cavazzoni, C.; de Gironcoli, S.; Delugas, P.; Ferrari Ruffino, F.; Ferretti, A.; Marzari, N.; Timrov, I.; Urru, A.; Baroni, S. QuantumESPRESSO toward the exascale. *J. Chem. Phys.* **2020**, *152*, 154105.
(65) Giannozzi, P.; et al. Advanced capabilities for materials modelling with Quantum ESPRESSO. *J. Phys.: Condens. Matter* **2017**, *29*, 465901.
(66) Prandini, G.; Marrazzo, A.; Castelli, I. E.; Mounet, N.; Marzari, N. Precision and efficiency in solid-state pseudopotential calculations. *npj Comput. Mater.* **2018**, *4*, 72.
(67) Lejaeghere, K.; et al. Reproducibility in density functional theory calculations of solids. *Science* **2016**, *351*, aad3000.
(68) Momma, K.; Izumi, F. VESTA 3 for Three-Dimensional Visualization of Crystal, Volumetric and Morphology Data. *J. Appl. Crystallogr.* **2011**, *44*, 1272−1276.
(69) Bernotat-Wulf, H.; Hoffmann, W. Die Kristallstrukturen der Bleiniobate vom Pyrochlor-Typ. *Z. für Kristallogr.—Cryst. Mater.* **1982**, *158*, 101−118.
(70) Shoemaker, D. P.; Seshadri, R.; Tachibana, M.; Hector, A. L. Incoherent Bi off-centering in $Bi_2Ti_2O_6O'$ and $Bi_2Ru_2O_6O'$: Insulator versus metal. *Phys. Rev. B: Condens. Matter Mater. Phys.* **2011**, *84*, 064117.
(71) Blaha, P.; Singh, D. J.; Schwarz, K. Geometric Frustration, Electronic Instabilities, and Charge Singlets in $Y_2Nb_2O_7$. *Phys. Rev. Lett.* **2004**, *93*, 216403.
(72) Talanov, M. V.; Talanov, V. M. Structural Diversity of Ordered Pyrochlores. *Chem. Mater.* **2021**, *33*, 2706−2725.
(73) Trump, B. A.; Koohpayeh, S. M.; Livi, K. J. T.; Wen, J.-J.; Arpino, K. E.; Ramasse, Q. M.; Brydson, R.; Feygenson, M.; Takeda, H.; Takigawa, M.; Kimura, K.; Nakatsuji, S.; Broholm, C. L.; McQueen, T. M. Universal Geometric Frustration in Pyrochlores. *Nat. Commun.* **2018**, *9*, 2619.
(74) Bailey, O.; Husremovic, S.; Murphy, M.; Ross, J.; Gong, J.; Olds, D.; Laurita, G. Compositional influence of local and long-range polarity in the frustrated pyrochlore system Bi2xRExTi2O7 (RE = Y3+,Ho3+). *J. Mater. Chem. C* **2022**, *10*, 13886.
(75) Safarik, D. J.; Schwarz, R. B.; Hundley, M. F. Similarities in the C_p/T^3 Peaks in Amorphous and Crystalline Metals. *Phys. Rev. Lett.* **2006**, *96*, 195902.
(76) Melot, B. C.; Tackett, R.; O'Brien, J.; Hector, A. L.; Lawes, G.; Seshadri, R.; Ramirez, A. P. Large low-temperature specific heat in pyrochlore $Bi_2Ti_2O_7$. *Phys. Rev. B: Condens. Matter Mater. Phys.* **2009**, *79*, 224111.
(77) Kennedy, B. J.; Ablott, T. A.; Avdeev, M.; Carter, M. L.; Losurdo, L.; Saura-Muzquiz, M.; Thorogood, K. J.; Ting, J.; Wallwork, K. S.; Zhang, Z.; Zhu, H.; Thorogood, G. J. Synthesis and Structure of

https://doi.org/10.1021/acs.inorgchem.2c03031
Inorg. Chem. 2022, 61, 18601−18610

Oxygen Deficient Lead-Technetium Pyrochlore, the First Example of a Valence V Technetium Oxide. *Front. Chem.* **2021**, *9*, 706269.
(78) Sleight, A. W. High pressure synthesis of platinum metal pyrochlores of the type Pb2M2O6−7. *Mater. Res. Bull.* **1971**, *6*, 775−780.
(79) Abakumov, A.; Shpanchenko, R.; Antipov, E.; Kopnin, E.; Capponi, J.; Marezio, M.; Lebedev, O.; Van Tendeloo, G.; Amelinckx, S. Synthesis and Structural Study of Pb2Re2O7xPyrochlores. *J. Solid State Chem.* **1998**, *138*, 220−225.
(80) Reading, J.; Knee, C. S.; Weller, M. T. Syntheses, structures and properties of some osmates(iv,v) adopting the pyrochlore and weberite structures. *J. Mater. Chem.* **2002**, *12*, 2376−2382.
(81) Kennedy, B. J. Oxygen Vacancies in Pyrochlore Oxides: Powder Neutron Diffraction Study of $Pb_2Ir_2O_{6.5}$ and $Bi_2Ir_2O_{7-2y}$. *J. Solid State Chem.* **1996**, *123*, 14−20.

https://doi.org/10.1021/acs.inorgchem.2c03031
Inorg. Chem. 2022, 61, 18601−18610